

# Frustrated Octahedral Tilting Distortion in the Incommensurately Modulated $\text{Li}_{3x}\text{Nd}_{2/3-x}\text{TiO}_3$ Perovskites

Artem M. Abakumov,<sup>\*,†</sup> Rolf Erni,<sup>‡</sup> Alexander A. Tsirlin,<sup>§</sup> Marta D. Rossell,<sup>‡</sup> Dmitry Batuk,<sup>†</sup> Gwilherm Nénert,<sup>||</sup> and Gustaaf Van Tendeloo<sup>†</sup>

<sup>†</sup>EMAT, University of Antwerp, B-2020 Antwerp, Belgium

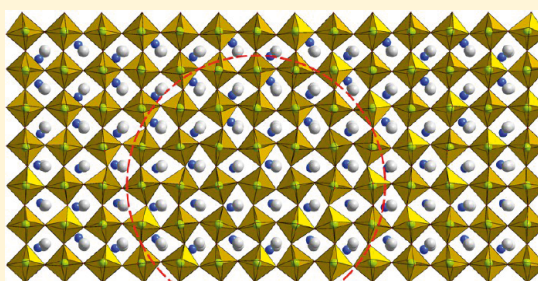
<sup>‡</sup>Electron Microscopy Center, Empa, Swiss Federal Laboratories for Materials Science and Technology, CH-8600 Dübendorf, Switzerland

<sup>§</sup>National Institute of Chemical Physics and Biophysics, 12618 Tallinn, Estonia

<sup>||</sup>Institut Laue Langevin, 6 rue Jules Horowitz, 38042 Grenoble, France

## Supporting Information

**ABSTRACT:** Perovskite-structured titanates with layered A-site ordering form remarkably complex superstructures. Using transmission electron microscopy, synchrotron X-ray and neutron powder diffraction, and ab initio structure relaxation, we present the structural solution of the incommensurately modulated  $\text{Li}_{3x}\text{Nd}_{2/3-x}\text{TiO}_3$  perovskites ( $x = 0.05$ , superspace group  $Pmmm(\alpha_1, 1/2, 0)000(1/2, \beta_2, 0)000$ ,  $a = 3.831048(5)$  Å,  $b = 3.827977(4)$  Å,  $c = 7.724356(8)$  Å,  $\mathbf{q}_1 = 0.45131(8)\mathbf{a}^* + 1/2\mathbf{b}^*$ ,  $\mathbf{q}_2 = 1/2\mathbf{a}^* + 0.41923(4)\mathbf{b}^*$ ). In contrast to earlier conjectures on the nanoscale compositional phase separation in these materials, all peculiarities of the superstructure can be understood in terms of displacive modulations related to an intricate octahedral tilting pattern. It involves fragmenting the pattern of the out-of-phase tilted  $\text{TiO}_6$  octahedra around the  $a$ - and  $b$ -axes into antiphase domains, superimposed on the pattern of domains with either pronounced or suppressed in-phase tilt component around the  $c$ -axis. The octahedral tilting competes with the second order Jahn–Teller distortion of the  $\text{TiO}_6$  octahedra. This competition is considered as the primary driving force for the modulated structure. The A cations are suspected to play a role in this modulation affecting it mainly through the tolerance factor and the size variance. The reported crystal structure calls for a revision of the structure models proposed for the family of layered A-site ordered perovskites exhibiting a similar type of modulated structure.



**KEYWORDS:** lithium neodymium titanium oxide, titanate, layered perovskite, phase separation, incommensurately modulated structure, octahedral tilting, A-site ordering, synchrotron X-ray diffraction, neutron diffraction, transmission electron microscopy

## INTRODUCTION

The unique flexibility of the perovskite structure enables large variations in the chemical composition and atomic arrangement, thus giving rise to a multitude of magnetic, dielectric, electronic, and catalytic properties. The majority of  $\text{ABX}_3$  perovskites departs from the cubic structure because different types of instabilities drive the structure toward lower symmetry.<sup>1</sup> These distortions are caused by cooperative tilts of nearly rigid  $\text{BX}_6$  octahedra to accommodate the A-X/B-X distance mismatch and/or by deformations of these octahedra following electronic effects on the B site, a displacement of the X atoms (Jahn–Teller effect for B-cations with partially filled d shell) or an off-center displacement of the B cations (second-order Jahn–Teller (SOJT) effect for the  $d^0$  B-cations). Combinations of competing distortion modes can cause remarkably high structure complexity because of the formation of modulated structures, for example, in multiferroic  $\text{EuTiO}_3$  and  $\text{Bi}_{0.75}\text{La}_{0.25}\text{FeO}_3$ ,<sup>2,3</sup> where the cooperative octahedral tilting strives with polar B-site or A-site displacements, respectively.

Different distortion modes superimposed on the partial or complete order of different cations and/or vacancies at the A or B sites complicate the structure even further. For example, perovskites with a mixture of cations on the B site, as in  $\text{PbMg}_{1/3}\text{Nb}_{2/3}\text{O}_3$ , are ferroelectric relaxors and good piezoelectrics. Their functional properties originate from polar nanoregions that can not be described in terms of fully ordered and periodic crystal structures, and require an alternative description at the local level.<sup>4</sup>

When the B position of the perovskite structure is filled by a single type of  $d^0$  cation, a mixed occupation of the A-site is still possible. If two distinct A and A' cations order, this will be almost inevitably a layered ordering. The preference of the A cations toward the layered arrangement was discussed in refs 5 and 6, using bond valence sum arguments. Layered A-site

Received: April 14, 2013

Revised: May 30, 2013

Published: June 4, 2013

ordering enables 2/3 of the oxygen atoms in the (BO<sub>2</sub>) layers to shift and optimize their coordination environment. However, such optimization is not possible for the 1/6 of the oxygen atoms in the (AO) and (A'O) layers, thus resulting in bonding instability. To relieve this bonding instability, B cations can be shifted (see Figure 12 from ref 5). The B cations acquire in turn an asymmetric octahedral coordination with one short, one long, and four medium B–O distances. This picture is typical for off-center displacements driven by the SOJT effect inherent to d<sup>0</sup> transition metal cations. The coupling of the layered A-site ordering and B-site off-center displacements has a synergetic effect. It leads to an antipolar structure with the off-center B-site displacements directed toward the (A'O) layers, where the A' cation carries a formal charge smaller than that of the A cation. Typically, the necessary charge difference between the A and A' cations is created through a population of the A positions by a trivalent lanthanide cation and the A' position by monovalent alkali metal cation and/or cation vacancy. Such perovskites have been widely studied owing to their technological importance as room temperature Li-ion conductors,<sup>7</sup> microwave dielectric ceramics,<sup>8</sup> and potential multiferroics.<sup>9,10</sup> Because of the peculiar nanometer-scale periodic phase separation pattern in Li<sub>3x</sub>Nd<sub>2/3-x</sub>TiO<sub>3</sub>, these perovskites were proposed as intriguing templates for the assembly of nanostructures or molecular monolayers.<sup>11</sup>

Although the crystal structure of the Li<sub>3x</sub>Nd<sub>2/3-x</sub>TiO<sub>3</sub> (Ln, lanthanide cation) perovskites has been intensively investigated, details of the atomic arrangement in these materials are still poorly understood. These compounds belong to the cation-deficient A-site ordered layered AA'B<sub>2</sub>O<sub>6</sub> perovskites, where the cation positions in the (AO) perovskite layer are taken by the Ln cation and the positions in the (A'O) are jointly occupied by Ln, Li, and cation vacancies. The ordered alternation of the (AO) and (A'O) layers doubles one of the perovskite unit cell parameters.<sup>12</sup> On top of this  $a_p \times a_p \times 2a_p$  ( $a_p$  being the parameter of the perovskite subcell) superstructure, a complex incommensurate ordering occurs, with two modulation vectors having the irrational components along either the **a**\* or **b**\* axis. The complexity of the Li<sub>3x</sub>Nd<sub>2/3-x</sub>TiO<sub>3</sub> ( $0.047 < x < 0.151$ )<sup>12,13</sup> materials was first noticed by García-Martín et al. who proposed that nanoscale twinning could be responsible for this modulation induced by domains with a uniform pattern of tilted TiO<sub>6</sub> octahedra separated by twin boundaries.<sup>13</sup> On the basis of transmission electron microscopy observations, Guiton and Davies suggested that a compositional phase separation occurs in Li<sub>3x</sub>Nd<sub>2/3-x</sub>TiO<sub>3</sub> and coexists with the twinned pattern of cooperatively tilted TiO<sub>6</sub> octahedra.<sup>11,14</sup> The alleged phase separation is reminiscent of a spinodal decomposition: it fragments the structure into a well-defined periodic nanoscale pattern of domains with tentative Nd<sub>2/3</sub>TiO<sub>3</sub> and Li<sub>1/2</sub>Nd<sub>1/2</sub>TiO<sub>3</sub> composition. The idea of a compositional phase separation was used as a background for interpreting the microstructural features in Li<sub>0.42</sub>Nd<sub>0.527</sub>TiO<sub>3</sub> and further tuning the structure model by the analysis of the Li displacements using bond valence sum arguments.<sup>15,16</sup>

As the application of Li<sub>3x</sub>Nd<sub>2/3-x</sub>TiO<sub>3</sub> perovskites requires precise knowledge of their crystal structure, and only qualitative models based on transmission electron microscopy observations were available so far, we have attempted a quantitative structure solution for the Li<sub>3x</sub>Nd<sub>2/3-x</sub>TiO<sub>3</sub> perovskites using the formalism of multidimensional crystallography. We found that the concept of compositional phase separation is not consistent with the experimental data. Therefore, we developed an

alternative structural model, which is based on displacive modulations only and entails a uniform chemical composition of these perovskites. The refined Li<sub>0.15</sub>Nd<sub>0.617</sub>TiO<sub>3</sub> crystal structure is fundamentally different from earlier proposals which revolved around the conjecture of a compositional phase separation. Using a combination of synchrotron X-ray and neutron powder diffraction data, transmission electron microscopy, and ab initio structure relaxation, we argue that the complex superstructure observed in the Li<sub>3x</sub>Nd<sub>2/3-x</sub>TiO<sub>3</sub> perovskites can be fully explained in terms of displacive modulations originating from a complex pattern of frustrated octahedral tilts that compete with a SOJT-driven distortion of the TiO<sub>6</sub> octahedra. Our results shed new light on the origin of modulated structures in a large group of perovskite compounds with similar phenomenology, including fast Li-ion conductors, dielectric materials for microwave electroceramics and potential multiferroics.

## ■ EXPERIMENTAL SECTION

Li<sub>3x</sub>Nd<sub>2/3-x</sub>TiO<sub>3</sub> samples with  $x = 0.05, 0.08, 0.12, 0.14$  have been prepared using solid state reaction between Li<sub>2</sub>CO<sub>3</sub>, Nd<sub>2</sub>O<sub>3</sub>, and TiO<sub>2</sub>. Before using, Nd<sub>2</sub>O<sub>3</sub> was dried by annealing at 800 °C for 20 h. The reagents were weighed in stoichiometric amounts, ground under acetone, and pressed into pellets. To prevent Li loss during the thermal treatment, the pellets were placed inside a powder of the same chemical composition with a mass of 3–5 times larger than the mass of the pellet. The powder and the pellet were annealed in alumina crucibles in air. The samples were heated up to 1050 °C at a rate of 150 °C/h and annealed for 24 h. Then the temperature was raised to 1250 °C followed by a further annealing for 24 h and cooling down to 600 °C at a rate of 10 °C/h. Finally, the samples were furnace cooled down to room temperature. The pellets were extracted and used for further analysis. The Nd/Ti atomic ratio in the prepared samples was measured using energy-dispersive X-ray analysis performed with a JEOL5510 scanning electron microscope equipped with an INCAx-sight 6587 system (Oxford instruments).

X-ray powder diffraction (XRPD) patterns were taken with a Philips X'pert diffractometer (CuK<sub>α</sub> radiation, reflection mode) and a Huber G670 Guinier diffractometer (CuK<sub>α1</sub> radiation, transmission mode). High-resolution synchrotron X-ray powder diffraction (SXPd) data were collected at the ID31 beamline of the European Synchrotron Radiation Facility (ESRF, Grenoble, France) using a constant wavelength of  $\lambda \approx 0.4$  Å and eight scintillation detectors, each preceded by a Si (111) analyzer crystal, in the angular range of  $2\theta = 1$ –40 deg. The powder sample was placed in a thin-walled borosilicate glass capillary that was spun during the experiment.

Room-temperature neutron powder diffraction (NPD) data for the  $x = 0.05$  sample were collected on the D2B high-resolution powder diffractometer at the Institut Laue Langevin (Grenoble, France). The sample was loaded in a vanadium container of 11 mm in diameter. The measurements were carried out at a wavelength of 1.594 Å corresponding to the (335) Bragg reflection of a germanium monochromator. The neutron detection was performed with <sup>3</sup>He counting tubes spaced at 1.25° intervals, and a complete diffraction pattern was obtained after about 25 steps of 0.05° in  $2\theta$ . Two data banks (high resolution and high intensity) were used, which differ by a fraction of the Debye–Scherrer rings used for integration. Rietveld refinement of the crystal structure was performed with the JANA2006 program.<sup>17</sup>

Transmission electron microscopy (TEM) was performed on crushed samples deposited on holey carbon grids. Electron diffraction (ED) patterns and high resolution TEM (HRTEM) images were acquired with a Tecnai G2 microscope operating at 200 kV. Bright field (BF), annular dark field (ADF), and high angle annular dark field (HAADF) scanning TEM (STEM) imaging was carried out using a JEOL JEM2200 fs microscope operated at 200 kV using a convergence semiangle of 10.8 mrad. Considering a spherical aberration of 1 mm and a defocus of –50 nm, this setting results in a STEM resolution of

about 0.16 nm. The HAADF inner detection semiangle was 100 mrad, and for ADF imaging an inner detection semiangle of 35 mrad was employed. ED patterns, HRTEM images, BF-STEM, HAADF-STEM images have been calculated using JEMS and xHREM software employing the Weickenmeier-Kohl scattering cross sections including thermal diffuse scattering.

The structural model derived from the X-ray and neutron diffraction data was compared to crystal structures relaxed within periodic density functional theory (DFT) band structure calculations for different supercells up to  $10a_p \times 10a_p \times 2a_p$  (950 atoms) with different spatial arrangements of the Nd and Li atoms. The spin-unpolarized calculations were performed in the VASP code using the projector-augmented-wave basis set and the Perdew–Burke–Ernzerhof flavor of the exchange–correlation potential.<sup>18–22</sup> Nd 4f orbitals were treated as core states. Residual forces in the relaxed crystal structures are below 0.02 eV/Å.

## RESULTS

### Unit Cell Parameters and Modulation Vectors.

Laboratory XRPD investigation confirmed the formation of single-phase  $\text{Li}_{3x}\text{Nd}_{2/3-x}\text{TiO}_3$  samples with  $x = 0.05, 0.08, 0.12, 0.14$ . The Nd/Ti atomic ratio measured by EDX analysis agrees with the bulk sample composition in the range of one standard deviation (Supporting Information, Table S1). The XRPD patterns readily suggest a perovskite structure with lattice parameters  $a \approx b \approx a_p$ ,  $c \approx 2a_p$ . The high-resolution SXPd patterns clearly reveal a perovskite subcell distortion mode for each composition (Figure 1). For the smallest Li content ( $x = 0.05$ ), an orthorhombic distortion is evident from the splitting of the  $h0l/0kl$  reflections (see 200/020 and 201/021 reflections exemplified in Figure 1b). The orthorhombic splitting decreases with increasing Li content, and vanishes for  $x = 0.12$  and  $x =$

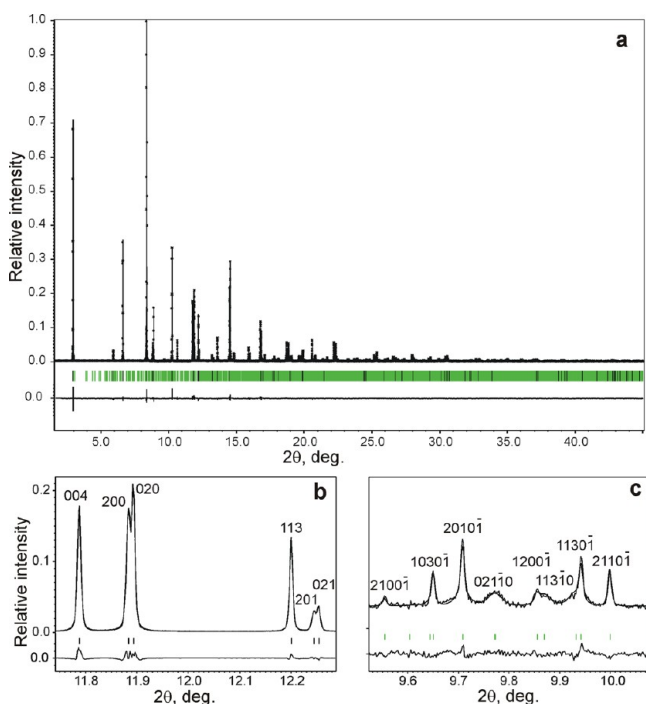


**Figure 1.** Synchrotron X-ray powder diffraction profile after the Rietveld refinement of the  $\text{Li}_{0.15}\text{Nd}_{0.617}\text{TiO}_3$  structure (a) and the illustration of the reflection splitting due to orthorhombic distortion of the basic unit cell (positions of satellites are not marked) (b) and positions and indexes of the brightest satellites (c).

0.14 so that the unit cell for these samples can be considered as metrically tetragonal.

[001] ED patterns demonstrate the presence of satellite reflections positioned close to the basic spots and the  $1/2\langle hk0 \rangle$ ,  $h, k$  - odd positions (Figure 2). The satellites can be indexed in

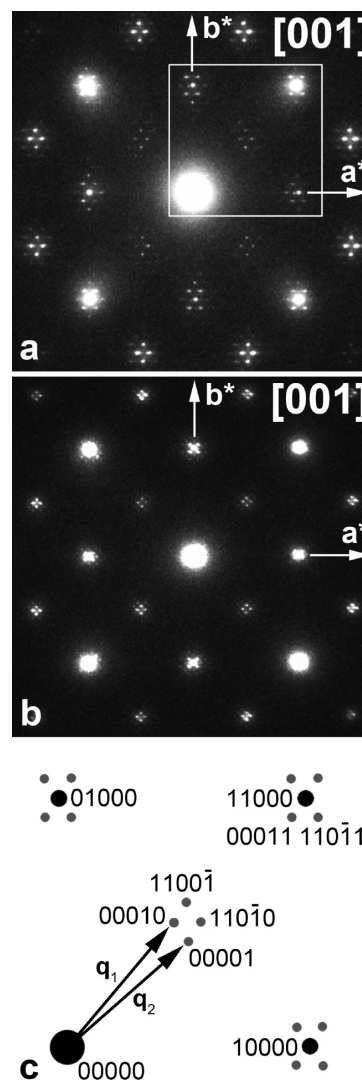


**Figure 2.** [001] ED patterns of  $\text{Li}_{0.15}\text{Nd}_{0.617}\text{TiO}_3$  (a) and  $\text{Li}_{0.42}\text{Nd}_{0.527}\text{TiO}_3$  (b) and the indexing scheme for the  $\text{Li}_{0.15}\text{Nd}_{0.617}\text{TiO}_3$  pattern (c). A fraction of the panel 2a (marked with a square) is reproduced in panel 2c. Only basic reflections and satellites with  $|m|, |n| = 1$  are indexed.

a  $(3 + 2)$ -dimensional approach assuming the diffraction vector  $\mathbf{H} = h\mathbf{a}^* + k\mathbf{b}^* + l\mathbf{c}^* + m\mathbf{q}_1 + n\mathbf{q}_2$ , with the modulation vectors  $\mathbf{q}_1 = \alpha_1\mathbf{a}^* + 1/2\mathbf{b}^*$  and  $\mathbf{q}_2 = 1/2\mathbf{a}^* + \beta_2\mathbf{b}^*$ , where both  $\alpha_1$  and  $\beta_2$  are slightly smaller than 1/2 (as suggested in ref 23). This indexing is also in agreement with the reciprocal lattice reconstruction performed by Garcia-Martin et al.<sup>13</sup> With this choice of the modulation vectors, no reflection conditions are observed from the ED patterns, which suggests  $Pmmm$  and  $P4/mmm$  space groups for the basic structure of the  $x = 0.05, 0.08$  and  $x = 0.12, 0.14$  materials, respectively. The actual  $(3 + 2)$ D superspace symmetry can not be unambiguously derived at this stage because of multiple diffraction effects (see Supporting Information, Figure S1) and will be determined in the course of the Rietveld refinement later. On the [001] ED pattern of



$\text{Li}_{0.15}\text{Nd}_{0.617}\text{TiO}_3$ , the satellite positions reflect unequal  $\alpha_1$  and  $\beta_2$  irrational components of the  $\mathbf{q}_1$  and  $\mathbf{q}_2$  modulation vectors ( $\alpha_1 > \beta_2$ ), in agreement with the proposed orthorhombic symmetry (Figure 2a,c). For tetragonal  $\text{Li}_{0.42}\text{Nd}_{0.527}\text{TiO}_3$  the  $\alpha_1$  and  $\beta_2$  components are equal, as can be seen from the positions of the satellites at the nodes of the square lattice (Figure 2b).

Inspection of the SXP patterns of  $\text{Li}_{3x}\text{Nd}_{2/3-x}\text{TiO}_3$  reveals weak satellite reflections, which can be indexed with the  $\mathbf{q}_1$  and  $\mathbf{q}_2$  modulation vectors compatible with the ED data. Surprisingly, the overwhelming majority of satellites can be indexed using the  $\mathbf{q}_2$  modulation vector only (Figure 1c). These satellites are sharper and most prominent on the SXP pattern. The satellites attributed to the  $\mathbf{q}_1$  modulation vector are substantially more diffuse; only a few of them can be unambiguously observed (Figure 1c). Such pronounced difference in the broadening of the  $\mathbf{q}_1$  ( $n = 0$ ) and  $\mathbf{q}_2$  ( $m = 0$ ) satellites can be attributed to random perturbations in the modulation wave associated with the  $\mathbf{q}_1$  vector and to the absence of such defects for the  $\mathbf{q}_2$  modulation. This assumption is directly confirmed by HRTEM observations (Figure 3). On

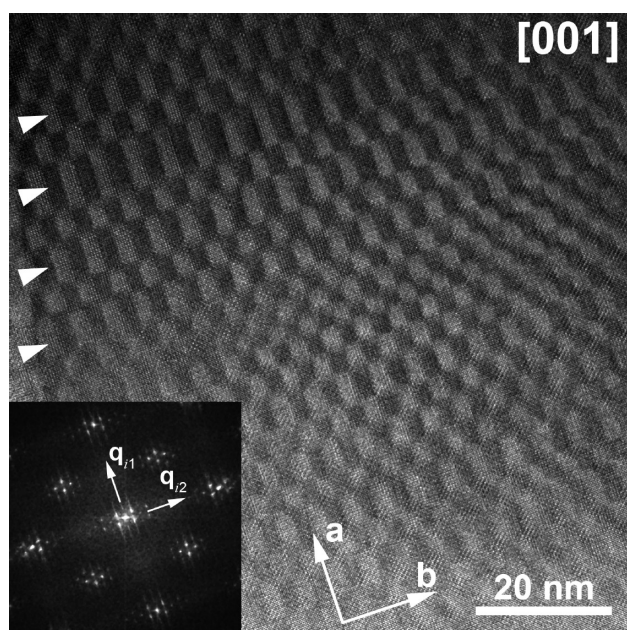


**Figure 3.** [001] HRTEM image of  $\text{Li}_{0.15}\text{Nd}_{0.617}\text{TiO}_3$  and corresponding Fourier transform. The modulation appears on the image as a pattern of rectangular domains with different brightness. Note the constant size of the domains in the  $b \parallel \mathbf{q}_2$  direction and the variable size in the  $a \parallel \mathbf{q}_1$  direction (marked with arrowheads). The satellites associated with  $\mathbf{q}_1$  appear streaked on the Fourier transform.

the [001] HRTEM image of  $\text{Li}_{0.15}\text{Nd}_{0.617}\text{TiO}_3$ , the modulation appears as a pattern of rectangular domains with different brightness. The domains feature a constant size along the  $b$ -axis, which is parallel to the direction of the irrational component  $\mathbf{q}_2$ . At the same time, the domains demonstrate variable size along the  $a$  axis parallel to the  $\mathbf{q}_1$  direction, indicating local violations in the periodicity of the modulation. These violations render the  $\mathbf{q}_1$  satellites streaked on the Fourier transform and underlie the large broadening of the  $\mathbf{q}_1$  satellites on the SXP pattern.

The unit cell parameters and components of the modulation vectors refined for different chemical compositions and

temperatures are listed in the Supporting Information, Table S2.

**STEM Analysis of the Phase Separation into the Li-Rich and Nd-Rich Domains.** Using the structure model constructed by Guiton and Davies (see Table S3 of Supporting Information for ref 11), we have performed simulations of the [001] bright field (BF) and high angle annular dark field (HAADF) STEM images. As expected, strong contrast features are observable both in the simulated BF- and HAADF-STEM images: the  $\text{Nd}_{2/3}\text{TiO}_3$  phase forms a zigzag pattern aligned along the  $\{110\}$  lattice planes of the basic  $a_p \times a_p \times 2a_p$  structure (Supporting Information, Figure S2). The zigzag pattern delimits square regions of the conjectured  $\text{Li}_{1/2}\text{Nd}_{1/2}\text{TiO}_3$  phase, which look pronouncedly darker. The chemically sensitive HAADF signal approximately scales as the square of the atomic number ( $Z$ ) of the elements in the sample. Hence, the expected ratio in HAADF intensity between the Nd and Li atoms is  $(Z_{\text{Nd}}/Z_{\text{Li}})^2 = 400$ . This ratio explains the intensity difference between the  $\text{Nd}_{1/2}\text{Li}_{1/2}\text{TiO}_3$  and  $\text{Nd}_{2/3}\text{TiO}_3$  domains in the simulated HAADF-STEM image.

The contrast features in the simulated STEM images are in remarkable disagreement with the experimental [001] images for the  $\text{Li}_{3x}\text{Nd}_{2/3-x}\text{TiO}_3$  samples. While the [001] BF-STEM image from the *thin* area of the  $\text{Li}_{0.15}\text{Nd}_{0.617}\text{TiO}_3$  sample shows a faint rectangular line pattern along the [100] and [010] directions (Figure 4a), the compositionally sensitive HAADF-STEM image does not show any indication for a patterned structure (Figure 4b). The same observation has been made in the  $\text{Li}_{0.24}\text{Nd}_{0.587}\text{TiO}_3$  and  $\text{Li}_{0.36}\text{Nd}_{0.547}\text{TiO}_3$  samples (Supporting Information, Figure S3). Moreover, in the  $\text{Li}_{0.36}\text{Nd}_{0.547}\text{TiO}_3$  and  $\text{Li}_{0.15}\text{Nd}_{0.617}\text{TiO}_3$  samples in addition to the faint features in *thin* areas, there are distinct contrast features in BF- and ADF-STEM images of *thick* areas (Figure 4c,d, and Supporting Information, Figure S4a, b, d, e), whereas they are practically absent in the corresponding HAADF-STEM image (Figure 4e, Supporting Information, Figure S4c, f). Figure 4f shows the selected area electron diffraction pattern corresponding to Figure 4c–e.

Figure 4 demonstrates that there are no or only a faint contrast modulations observable in the chemically sensitive HAADF-STEM images, opposed to the strong contrast expected from simulated HAADF-STEM images of the model with a compositionally induced phase separation (Supporting Information, Figure S2). Yet, the “Z-contrast effect” reported by Guiton and Davies can be vaguely seen only in rather thick sample areas (see Figure 1c from ref 5). Moreover, compared to Guiton and Davies, we used a HAADF detection angle a factor of 2 larger, meaning that our HAADF-STEM images in Figure 4 are less affected by diffraction effects. Therefore, our images should be even more sensitive to any chemical contrast. Furthermore, it can be shown that the “Z-contrast effect” reported by Guiton and Davies increases with decreasing the HAADF detection angle (see Figure 4d,e), although in the scenario of compositional phase separation one would expect a completely opposite behavior.<sup>24</sup> This observation confirms that the contrast interpreted by Guiton and Davies as a compositional phase separation is not of chemical nature, but it is dominated by a diffraction effect, originating, for example, from the local channeling condition determined by the strain field associated with atomic displacements. Hence, the contrast features in the BF- and ADF-STEM images cannot be due to a separation into  $\text{Nd}_{2/3}\text{TiO}_3$  and  $\text{Li}_{1/2}\text{Nd}_{1/2}\text{TiO}_3$  domains.

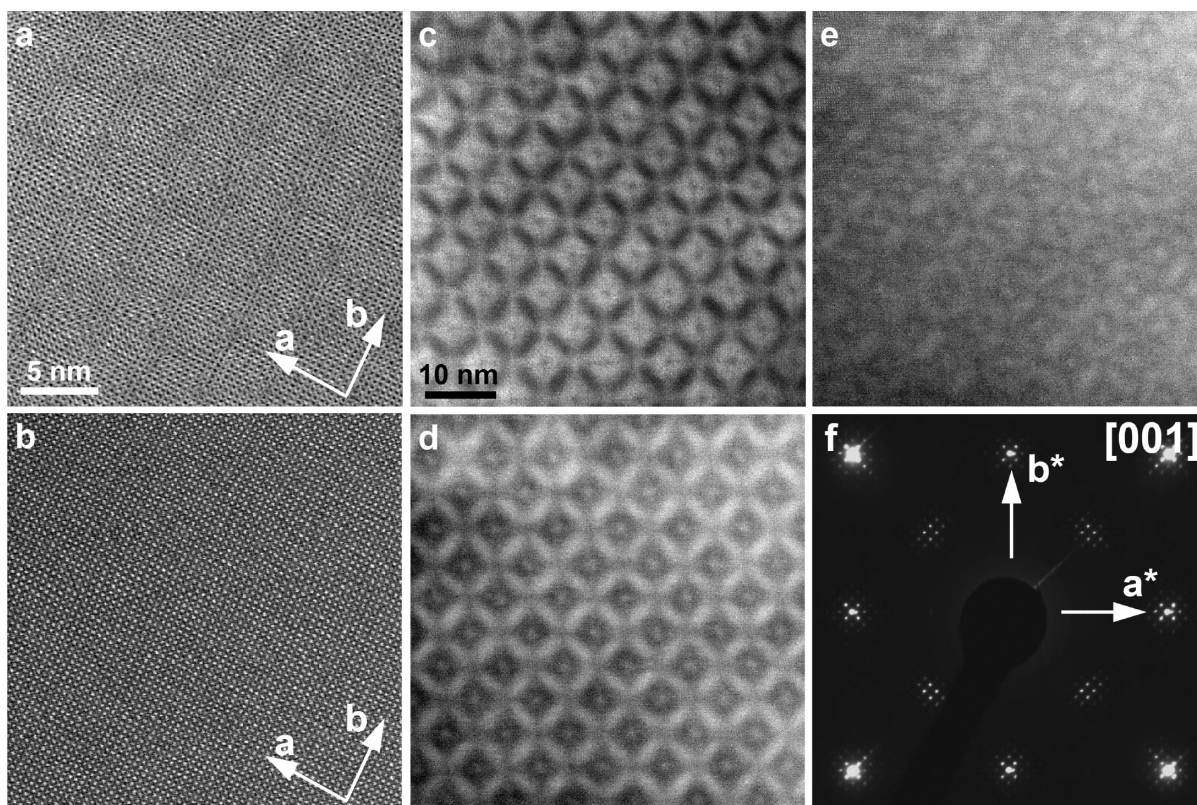


**Figure 4.**  $\text{Li}_{0.15}\text{Nd}_{0.617}\text{TiO}_3$  (thin area): simultaneously recorded [001] BF-STEM image (a) and HAADF-STEM image (b);  $\text{Li}_{0.36}\text{Nd}_{0.547}\text{TiO}_3$  (thick area): simultaneously recorded [001] BF-STEM image (c), ADF-STEM image (d), and the same area recorded in HAADF-STEM mode (e). (f) Electron diffraction pattern of  $\text{Li}_{0.36}\text{Nd}_{0.547}\text{TiO}_3$ . The inner detection angle for the ADF image was 35 mrad, and for the HAADF image 100 mrad. The claimed phase separation model of ref 11 would demand for a stronger contrast in the compositionally sensitive Z-contrast image obtained under HAADF STEM conditions, compared with the ADF STEM image. The dependence of the image contrast as a function of STEM detection angle (ADF vs HAADF) rules out the possibility of a compositional modulation.

The partially coherent BF-STEM image reveals the mapping of the distortion field as this is done complementary in bright-field zone-axis HRTEM imaging (see, e.g., ref 25). A very similar behavior of the contrast on the HAADF- and BF-STEM images was reported recently for the  $\text{Li}_{0.38}\text{Nd}_{0.54}\text{TiO}_3$  material.<sup>16</sup> Despite reporting the remarkably weak HAADF-STEM contrast and the strong contrast on the complementary BF-STEM image, Withers et al. still consider their observations in the context of compositional phase separation.

A further indication that the model of Guiton and Davies does not reflect all details of the structural organization of the  $\text{Li}_{3x}\text{Nd}_{2/3-x}\text{TiO}_3$  perovskites comes from a comparison between the experimental and calculated ED patterns. Dynamical simulations of the [001] ED patterns using the model of Guiton and Davies do not reproduce the experimental ED data (Supporting Information, Figure S5). Particularly, the simulation reveals dramatic discrepancies in the intensities of the satellite reflections decorating the  $1/2\langle hk0 \rangle$ ,  $h, k$  - odd positions. The model of Guiton and Davies produces zero intensity for these satellites, whereas they are clearly visible on the experimental ED patterns (Figure 2 and Supporting Information, Figure S5). This reflects that, first, the compositional modulation does not make any impact to these satellites and, second, some longitudinal displacive modulation wave, which is responsible for the nonzero intensity of these satellites, is not taken into account. For example, such missed modulation can originate from tilting of the  $\text{TiO}_6$  octahedra around the  $c$ -axis. However, the high complexity of this system allows for

different and potentially ambiguous qualitative interpretations of the TEM data. Therefore, we attempted quantitative characterization of the modulated structure of the  $\text{Li}_{3x}\text{Nd}_{2/3-x}\text{TiO}_3$  perovskites using (3 + 2)-dimensional crystallography combined with a joint Rietveld refinement from SXPD and NPD data.

**$\text{Li}_{0.15}\text{Nd}_{0.617}\text{TiO}_3$ : Structure Refinement.** Some important aspects concerning the superspace treatment of the  $\text{Li}_{3x}\text{Nd}_{2/3-x}\text{TiO}_3$  structures should be explicitly mentioned.

(1) The appearance of a modulation on the TEM images (Figures 3 and 4) in the form of rectangular domains with sharp, well-defined boundaries suggests that the atomic displacements would be best modeled with discontinuous modulation functions, such as, for example, a sawtooth function defined on atomic domains of restricted width. However, these modulation functions are not yet implemented for the structures with more than one modulation vector. Therefore, the structure has to be modeled with harmonic modulation functions only, taken in the following form:

$$U^\lambda(x_4, x_5) = \sum_m \sum_n [A_{s,m,n}^\lambda \sin(2\pi m x_4 + 2\pi n x_5) + B_{c,m,n}^\lambda \cos(2\pi m x_4 + 2\pi n x_5)] \quad (1)$$

where  $x_4 = \mathbf{q}_1 \mathbf{r}^\lambda + t$ ,  $x_5 = \mathbf{q}_2 \mathbf{r}^\lambda + u$ ,  $\mathbf{r}^\lambda$  is the position of the atom  $\lambda$  in the basic structure,  $t$  and  $u$  are internal phases.

(2) To model the abrupt change in the modulation functions at the domain boundaries, harmonics with high  $m$  and  $n$  would



be required. However, the use of powder diffraction data severely limits the maximum order of the harmonics. The satellites with  $|ml| + |nl| > 2$  are too weak to be detected on both SXPD and NPD patterns. At the same time, including higher-order satellites into the Rietveld refinement leads to a very dense set of reflections resulting in severe reflection overlap that makes the refinement virtually impossible. Thus, the structure has to be modeled with a restricted number of harmonic functions that unavoidably provide only a rough approximation. Nevertheless, main trends can be analyzed, at least in a semiquantitative manner.

The refinement of the basic  $a_p \times a_p \times 2a_p$  perovskite structure with the  $Pmmm$  space group was performed against SXPD and two NPD (high-resolution and high-intensity) data banks with the following set of the atomic positions: Nd1:  $1a$ ,  $0,0,0$ ; Nd2/Li:  $1c$ ,  $0,0,1/2$ ; Ti:  $2t$ ,  $1/2,1/2,z \approx 0.262$ ; O1:  $1f$ ,  $1/2,1/2,0$ ; O2:  $1h$ ,  $1/2,1/2,1/2$ ; O3:  $2r$ ,  $0,1/2,z \approx 0.241$ ; O4:  $2s$ ,  $1/2,0,z \approx 0.229$  (Figure 5). The refinement revealed good

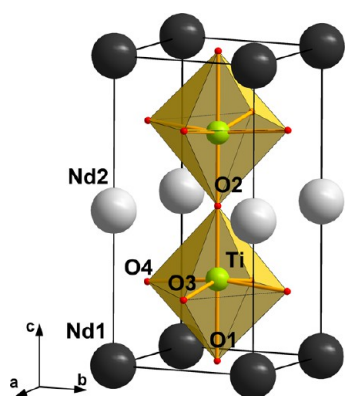


**Figure 5.** Basic structure of  $\text{Li}_{0.15}\text{Nd}_{0.617}\text{TiO}_3$ . Li atoms are not shown for clarity.

agreement between the experimental and the calculated SXPD profiles ( $R_F = 0.055$ ,  $R_p = 0.059$ ), whereas the fit of the NPD patterns was obviously much worse ( $R_F = 0.16$ ,  $R_p = 0.099$ ). This indicates that the major deviations from the basic structure pertain to the oxygen atoms, which provide a larger impact on the intensities of the NPD patterns in comparison with the synchrotron X-ray diffraction. Indeed, the refinement of the atomic displacement parameters (ADPs) revealed that the ADPs maintain reasonable values for the Nd1, Nd2/Li ( $\sim 0.011 \text{ \AA}^2$ ) and Ti ( $\sim 0.006 \text{ \AA}^2$ ) positions and become abnormally high for the O1–O4 positions ( $\sim 0.048$ – $0.066 \text{ \AA}^2$ ). Thus, one can expect that the primary modulation is confined to the displacements of the oxygen atoms.

For the refinement of the modulated structure, different  $(3 + 2)$ -dimensional superspace groups were tested, based on the space group  $Pmmm$  (see Supporting Information, Table S3). The solution has been found in the  $(3 + 2)$ D superspace group  $Pmmm(\alpha_1, 1/2, 0)000(1/2, \beta_2, 0)000$  (#47.2.35.57 in the Stokes–Campbell–van Smaalen notations,  $Pmmm(0, \beta_1, 1/2)000(0, 1/2, \gamma_2)000$  in a standard setting)<sup>26</sup> with the symmetry operators listed in the Supporting Information, Table S4. Further attempts to lower the symmetry to the acentric subgroups ( $P2mm$ ,  $Pm2m$ ,  $Pmm2$ ,  $P222$ ) did not improve the fit and resulted in an unjustified increase in the number of refineable parameters. To test the hypothesis of the compositional modulation in the mixed Nd2/Li position, the  $1c$  position was split into two positions occupied by the Nd and Li atoms,

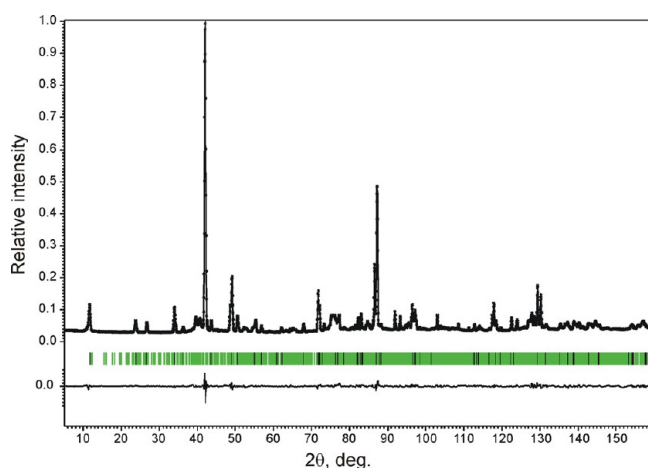
respectively, with the overall occupancies corresponding to the bulk  $\text{Li}_{0.15}\text{Nd}_{0.617}\text{TiO}_3$  composition. Harmonic occupational modulation waves were refined for each position independently, while keeping the same ADP for both positions. An attempt to include occupational modulation into the refinement was performed prior to the refinement of the amplitudes of displacive modulation waves, as well as after the displacive modulation was taken into account. In both cases the refinement of the occupancy modulation within the Nd2/Li layer did not improve the reliability factors. A close inspection of the diffraction profiles revealed that the occupancy modulation does not make any noticeable impact on the intensity of the satellite reflections. This is in agreement with the analysis of the  $\text{Li}_{0.25}\text{Nd}_{0.583}\text{TiO}_3$  NPD pattern by Guiton et al.<sup>14</sup> where the experimental NPD pattern revealed the absence of cation-dependent reflections predicted by the simulated NPD pattern of the 50%  $\text{Li}_{1/2}\text{Nd}_{1/2}\text{TiO}_3$ –50%  $\text{Nd}_{2/3}\text{TiO}_3$  phase separated model.

On the basis of these arguments, the hypothesis of an occupational modulation related to the compositional phase separation was rejected, and the model with displacive modulations only was considered for further refinement. For the Nd1, Nd2, Ti, and O1–O4 positions, the refinement of the harmonic modulation function coefficients converged smoothly, bringing the ADPs for the oxygen atoms back to normal values. However, the refinement was not very sensitive to the modulation parameters of the Li atom at the ideal perovskite A-position provides a satisfactory fit, but unreasonably short (up to  $\sim 1.3 \text{ \AA}$ ) and long ( $> 2.4 \text{ \AA}$ ) Li–O distances in some unit cells and a relatively high ADP of  $0.047 \text{ \AA}^2$ . In fact, displacement along the  $\langle 100 \rangle_p$  directions toward the square window formed by the oxygen atoms of the  $\text{BO}_6$  octahedra is suggested for the Li atoms at the A position of the perovskite structure.<sup>27,28</sup> Thus, Li displacements were introduced by shifting the Li atom from the special  $1c$  position toward the  $x, y, 1/2$  position, with the  $x$  and  $y$  coordinates being refined. The  $x$  coordinate deviates from 0 significantly (see Supporting Information, Table S5), whereas the  $y$  coordinate stays very close to 0, indicating preferentially one-dimensional Li displacements along the  $a$  axis. For the final refinement steps, the  $y$  coordinate of Li was fixed to 0, common ADPs were set for the Nd2 and Li atoms and the O1–O4 atoms, respectively. The coefficients of the modulation functions were fixed to zero if their values were below the standard deviation, and soft constraints were imposed on the Nd1–O distances. The refinement resulted in a very good agreement for the SXPD and two NPD patterns and low reliability factors for the main reflections and satellites. Selected crystallographic parameters for  $\text{Li}_{0.15}\text{Nd}_{0.617}\text{TiO}_3$  are listed in Table 1, atomic coordinates, ADPs and parameters of the modulation functions are given in Supporting Information, Table S5. The main interatomic distances are provided in Supporting Information, Table S6. The experimental, calculated, and difference SXPD and NPD profiles are shown in Figure 1a and 6, respectively.

The refined  $\text{Li}_{0.15}\text{Nd}_{0.617}\text{TiO}_3$  structure was additionally verified by the dynamical simulation of the  $[001]$  ED pattern, HRTEM, and STEM images. The ED simulation has been performed on a  $20a_p \times 20a_p \times 2a_p$  commensurate approximant. In contrast to the model of Guiton and Davies, the refined structure reproduces well the intensities of the satellite reflections, including those decorating the  $1/2\langle hk0 \rangle$ ,  $h$ ,  $k$  - odd positions (Supporting Information, Figure S6). Simulated

**Table 1.** Selected Crystallographic Data and Refinement Parameters for  $\text{Li}_{0.15}\text{Nd}_{0.617}\text{TiO}_3$ 

formula	$\text{Li}_{0.15}\text{Nd}_{0.617}\text{TiO}_3$
superspace group	$Pmmm(\alpha_1, 1/2, 0)000(1/2, \beta_2, 0)000$
$a$ , Å	3.831048(5)
$b$ , Å	3.827977(4)
$c$ , Å	7.724355(8)
$q_1$	$0.45130(8)a^* + 1/2b^*$
$q_2$	$1/2a^* + 0.41924(4)b^*$
calculated density, g/cm <sup>3</sup>	5.469
Z	2
radiation	synchrotron X-ray, $\lambda = 0.3962$ Å
$2\theta$ range, step, deg.	$2 \leq 2\theta \leq 50$ ; 0.002
$R_F$ (all, main reflections)	0.045, 0.026
$R_F$ (satellites of order 1, 2)	0.076, 0.065
$R_p$ , $R_{wp}$	0.047, 0.063
radiation	neutron (high intensity), $\lambda = 1.594$ Å
$2\theta$ range, step, deg.	$14 \leq 2\theta \leq 159$ ; 0.05
$R_F$ (all, main reflections)	0.028, 0.025
$R_F$ (satellites of order 1, 2)	0.030, 0.029
$R_p$ , $R_{wp}$	0.026, 0.033
radiation	neutron (high resolution), $\lambda = 1.594$ Å
$2\theta$ range, step, deg.	$5 \leq 2\theta \leq 159$ ; 0.05
$R_F$ (all, main reflections)	0.031, 0.028
$R_F$ (satellites of order 1, 2)	0.031, 0.035
$R_p$ , $R_{wp}$	0.032, 0.041

**Figure 6.** Neutron powder diffraction profile after the Rietveld refinement of the  $\text{Li}_{0.15}\text{Nd}_{0.617}\text{TiO}_3$  structure. Black and green bars mark the positions of the basic and satellite reflections, respectively.

[001] HRTEM images of the  $20a_p \times 12a_p \times 2a_p$  commensurate approximant (Supporting Information, Figure S7) reproduce the rectangular domain contrast (see Figure 3) and the “diamond-type” contrast as reported by Guiton and Davies, depending on crystal thickness and selected defocus. Moreover, BF-, ADF-, and HAADF-STEM simulations (Supporting Information, Figure S8) can fairly well reproduce the main characteristics of the experimental STEM images considering the limitation of the multislice method to model channeling effects that arise because of changes in the atomic spacing along the beam direction and because of the harmonic approximation of the rectangular pattern.

A commensurate approximant of the refined structure is based on the modulation vectors  $q_1 = 9/20a^* + 1/2b^*$  and  $q_2 = 1/2a^* + 5/12b^*$ . Possible 3D symmetries of the approximant

for different  $t$ ,  $u$  values are provided in Supporting Information, Table S7. The  $20a_p \times 12a_p \times 2a_p$  commensurate  $\text{Li}_{0.15}\text{Nd}_{0.617}\text{TiO}_3$  structure is shown in Figure 7. For the sake of clarity, only one of the two mirror-related Li positions  $x, 0, 1/2$  and  $-x, 0, 1/2$  is displayed. The tilting distortion of the octahedral perovskite framework is very obvious from Figure 7. The  $\text{TiO}_6$  octahedra are tilted around both  $a$ - and  $b$ -axes with variable modulated amplitude. Generally, these tilt components have an out-of-phase character and can be denoted as  $a^-$ ,  $b^-$  using Glazer's notations (note, however, that Glazer's notations are not strictly applicable to the structure with the variable tilt amplitude, such as  $\text{Li}_{0.15}\text{Nd}_{0.617}\text{TiO}_3$ ). A remarkable difference between the refined structure and the models proposed earlier is the presence of a tilt component around the  $c$ -axis.<sup>11,14,16</sup> The areas with the pronounced  $c$ -tilt component (marked with the red circles in Figure 7) interleave with areas where the  $c$ -tilt is suppressed. The amplitude of the  $c$ -tilt is maximal at the center of these regions and gradually decreases to the periphery. The  $c$ -tilt occurs in-phase, so that the overall tilt system can be represented as  $a^-b^-c^+$ . However, a more detailed analysis provided below demonstrates that this notation is only a coarse approximation of the complex interplay of the octahedral tilts in the  $\text{Li}_{0.15}\text{Nd}_{0.617}\text{TiO}_3$  structure.

The basic  $a_p \times a_p \times 2a_p$  structure implies a complete absence of the tilting distortion of the underlying perovskite framework.<sup>28</sup> Indeed, according to the group-theory analysis, a perovskite with the layered A-site ordering and  $a^-b^-c^+$  tilt system should demonstrate a monoclinic  $a_p\sqrt{2} \times a_p\sqrt{2} \times 2a_p$  superstructure, but no corresponding superlattice reflections are observed on the diffraction patterns of  $\text{Li}_{3x}\text{Nd}_{2/3-x}\text{TiO}_3$ . Instead, the satellite reflections appear at the incommensurately modulated positions, indicating that the  $a^-b^-c^+$  tilt system is subjected to periodic perturbations. A periodic twinning of the  $a$ - and  $b$ -tilts with the (010) and (100) twin planes, respectively, has been suggested as such perturbation.<sup>14</sup> Figure 8 shows the maps of the  $a$  and  $b$  tilt components in the  $\text{Li}_{0.15}\text{Nd}_{0.617}\text{TiO}_3$  structure, which are apparently more complex than the simplified picture of a periodic two-dimensional twinning. The map of the  $a$ -tilt consists of zigzag shaped domains with the prevailing out-of-phase  $a^-$  tilts. The tilting patterns in the neighboring domains are in antiphase relation to each other being shifted by the [010] vector of the basic unit cell. The antiphase boundaries (APB) between the domains have a complex structure. They consist of straight (100) parts, interleaving with the square regions shaped by the {110} lattice planes. The octahedra within these regions are either tilted in-phase or not tilted at all around the  $a$ -axis. Such regions can be considered as the areas of the  $a^+$  tilt component. A similar consideration can be applied to the map of the  $b$ -tilt, with the only difference that the APBs are confined to the (010) planes with the shift along [100], and the rectangular regions of the  $b^+$  tilt are shaped by the (100) and (010) lattice planes.

A remark should be made here clarifying the use of the terms “antiphase domains” and “antiphase boundaries”. Generally, these terms are associated with planar defects arising in periodic crystal structures, for example, because of the loss of translational symmetry in the course of continuous phase transitions.<sup>30,31</sup> In this context, these terms refer to the defect planes, which are irregularly spaced and separate domains of variable width. Here, we apply the term “antiphase boundary” to identify the interfaces between domains, which occur periodically, although their periodicity is incommensurate with the parent structure. Periodically spaced nonconservative



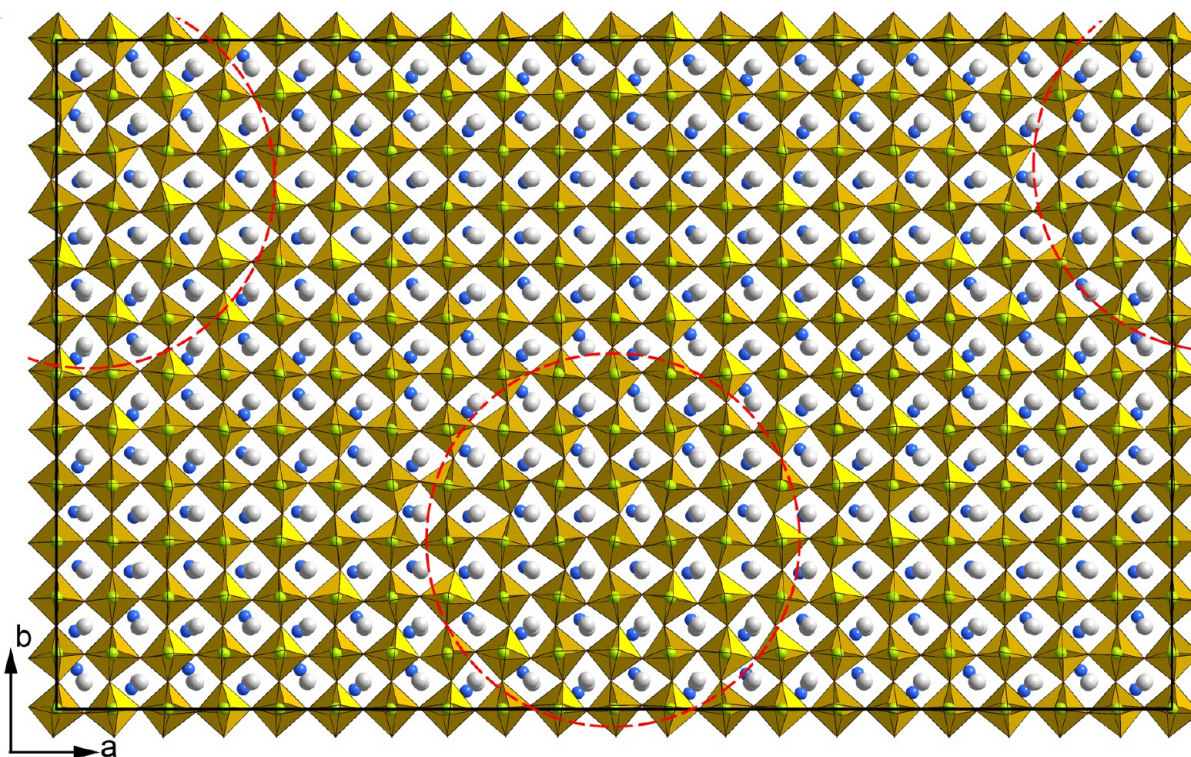


**Figure 7.**  $20a_p \times 12a_p \times 2a_p$  commensurate approximant of the  $\text{Li}_{0.15}\text{Nd}_{0.617}\text{TiO}_3$  structure. The Ti atoms (green spheres) are positioned in the oxygen octahedra. Nd and Li atoms are shown as gray and blue spheres, respectively. The red dashed circles mark the regions with a pronounced tilt of the  $\text{TiO}_6$  octahedra around the  $c$ -axis.

APBs (crystallographic shear planes) in perovskites are known to introduce compositionally modulated structures.<sup>32–35</sup> In the present case, the APBs are conservative and do not result in any change in the chemical composition.

The Ti–O distances were analyzed as a function of the fourth ( $t$ ) and fifth ( $u$ ) coordinate in superspace. A plot of the structural parameter value in the  $t$ - $u$  coordinates provides a comprehensive overview of the variation of this parameter in different unit cells of the basic structure (see ref 36). Such plots for the Ti–O distances are shown in Figure 9, where the length of the Ti–O bond is color-coded. Every point on the  $t$ - $u$  plot represents a unit cell in the physical 3D space, but two closely positioned points on the plot may represent unit cells that are far away from each other in the 3D space.

A comparison of the plots for the apical Ti–O1 (Figure 9a) and Ti–O2 (Figure 9b) distances reveals that a displacement of the Ti atom along the  $c$ -axis toward the (Nd,Li)O2 layer is present in all unit cells, since  $d(\text{Ti–O1}) > d(\text{Ti–O2})$  at any point of the  $t$ - $u$  plot. The Ti–O1 and Ti–O2 distances vary in the 2.016–2.084 Å and 1.814–1.924 Å range, respectively. Significant variations of the equatorial Ti–O3 (Figure 9c) and Ti–O4 (Figure 9d) distances are also observed:  $d(\text{Ti–O3}) = 1.89$ – $2.04$  Å,  $d(\text{Ti–O4}) = 1.86$ – $2.04$  Å. The areas with the minimal and maximal  $d(\text{Ti–O3})$  and  $d(\text{Ti–O4})$  do not exactly coincide on the  $t$ - $u$  plots: there are also areas with  $d(\text{Ti–O3}) \approx d(\text{Ti–O4})$ . Therefore, in the modulated  $\text{Li}_{0.15}\text{Nd}_{0.617}\text{TiO}_3$  structure, the Ti atoms are preferentially shifted toward the oxygen atoms along the  $[001]$ ,  $[011]$ ,  $[101]$ , and  $[111]$  perovskite directions. The degree of this distortion can be reflected by the octahedral distortion parameter  $\Delta d$  defined as

$$\Delta d = 1/6 \sum_{n=1-6} [(d_n - d)/d]^2 \quad (2)$$

where  $d_n$  is an individual Ti–O bond length and  $d$  is an average Ti–O bond length.<sup>37</sup> The  $t$ - $u$  plot of the octahedral distortion is shown in Figure 10a. Clear maxima on the  $\Delta d$  plot are visible. Since the displacement of the Ti atom along the  $c$ -axis can be considered as nearly constant for all unit cells, these maxima reflect the unit cells with the highest variance of the Ti–O distances in the  $a$ - $b$  plane. The positions of these maxima in the  $t$ - $u$  plot fall into the regions of smallest  $c^+$ -octahedral tilt angle (compare Figure 10a and 10b). This indicates an anticorrelation between the variation of the Ti–O3 and Ti–O4 distances and the  $c^+$  component of the octahedral tilt. The displacement of the Li atoms also anticorrelates with the  $c^+$  tilt component (Figure 10c). Indeed, the maximal amplitude of the octahedral tilt requires a smaller shift of the Li atom from the center of the perovskite cube to achieve reasonable Li–O interatomic distances.

**Ab Initio Structure Relaxation.** The modeling of the incommensurately modulated  $\text{Li}_{3x}\text{Nd}_{2/3-x}\text{TiO}_3$  structures requires large supercells that are capable of reproducing the different types of atomic displacements, as well as the relevant Nd/Li content that was set to the  $\text{Li}_{0.125}\text{Nd}_{0.625}\text{TiO}_3$  composition. Initially, we performed calculations for the  $6a_p \times 7a_p \times 2a_p$  supercell (334 atoms), where the convergence with respect to the number of  $k$  points could be carefully checked. The relaxations with a single  $k$ -point, 2  $k$ -points ( $1 \times 1 \times 2$  partitioning), and 8  $k$ -points ( $2 \times 2 \times 2$  partitioning) led to essentially indistinguishable results. Therefore, calculations for even larger supercells could be attempted under the constraint of using a single  $k$ -point. As  $\text{Li}_{3x}\text{Nd}_{2/3-x}\text{TiO}_3$  is a band insulator with a sizable band gap of about 2 eV, the convergence with respect to the  $k$  mesh is easily reached, and even a single  $k$ -point provides realistic results. Unfortunately, calculations of the 950-atom  $10a_p \times 10a_p \times 2a_p$  supercells with more than one



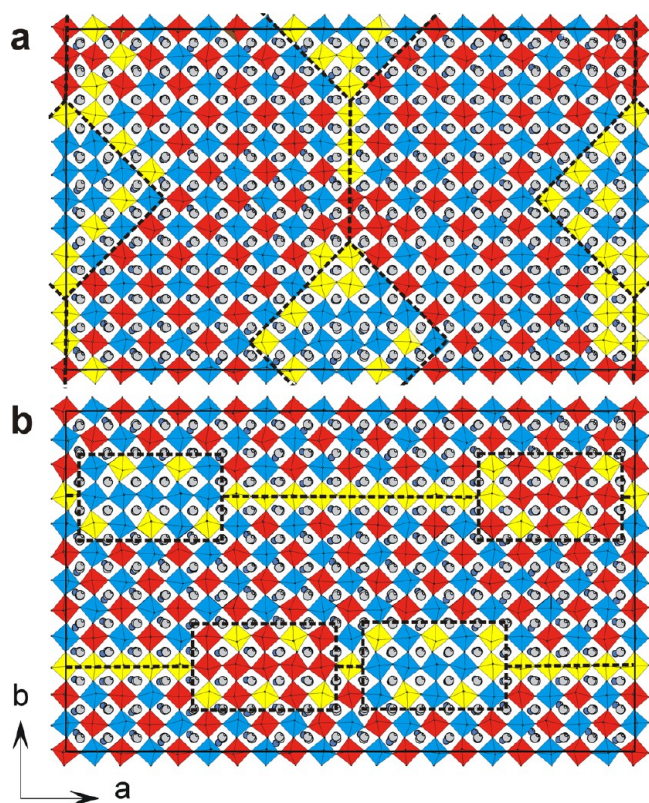


**Figure 8.** Maps of the  $a$  (a) and  $b$  (b) tilt components of the  $\text{TiO}_6$  octahedra in the  $\text{Li}_{0.15}\text{Nd}_{0.617}\text{TiO}_3$  structure. The maps reflect only the signs of the  $\text{TiO}_6$  octahedra rotations: the octahedra rotated in opposite directions are marked in red and blue, respectively. The octahedra marked in yellow either do not demonstrate the corresponding tilt or the amplitude of this tilt is so small that it is masked by the octahedral distortion. Dashed lines separate the domains of out-of-phase  $a$ - and  $b$ -tilts, as seen by the chessboard ordering patterns of the red and blue octahedra. The tilt patterns in neighboring domains are in antiphase relations. At the antiphase boundaries small square (a) or rectangular (b) regions are formed where the octahedra have the same tilt sign (i.e.,  $a^+$  or  $b^+$  regions).

$k$ -point remain computationally unfeasible. The structures relaxed within the 334-atom supercell feature off-center displacements of the Ti and Li cations, but they fail to reproduce the tilting of the  $\text{TiO}_6$  octahedra around the  $c$  axis, which is an important ingredient of our structural model. Therefore, larger supercells have to be considered. The  $c$ -component of the tilting can be reproduced in the 950-atom supercells with different arrangements of the Nd and Li atoms. We have performed relaxations for two types of the structure featuring ordered and random cation arrangement that resulted in the overall orthorhombic ( $P2mm$ ) and monoclinic ( $P11m$ ) symmetries, respectively. Both orthorhombic and monoclinic structures reveal the main features of our experimental structural model, as further explained in Discussion (see also Figure 11). The atomic coordinates and bond valence sum for the cations in the relaxed  $\text{Li}_{0.125}\text{Nd}_{0.625}\text{TiO}_3$  structure with the random cation arrangement are provided in the Supporting Information, Table S8. There is a minor energy difference of 33 meV/f.u. between the two models, with a slight preference for the random cation arrangement. While the exact value of this energy difference should be taken with caution, because calculations are performed for one  $k$ -point only, our results rule out any large energy gain related to cation ordering.

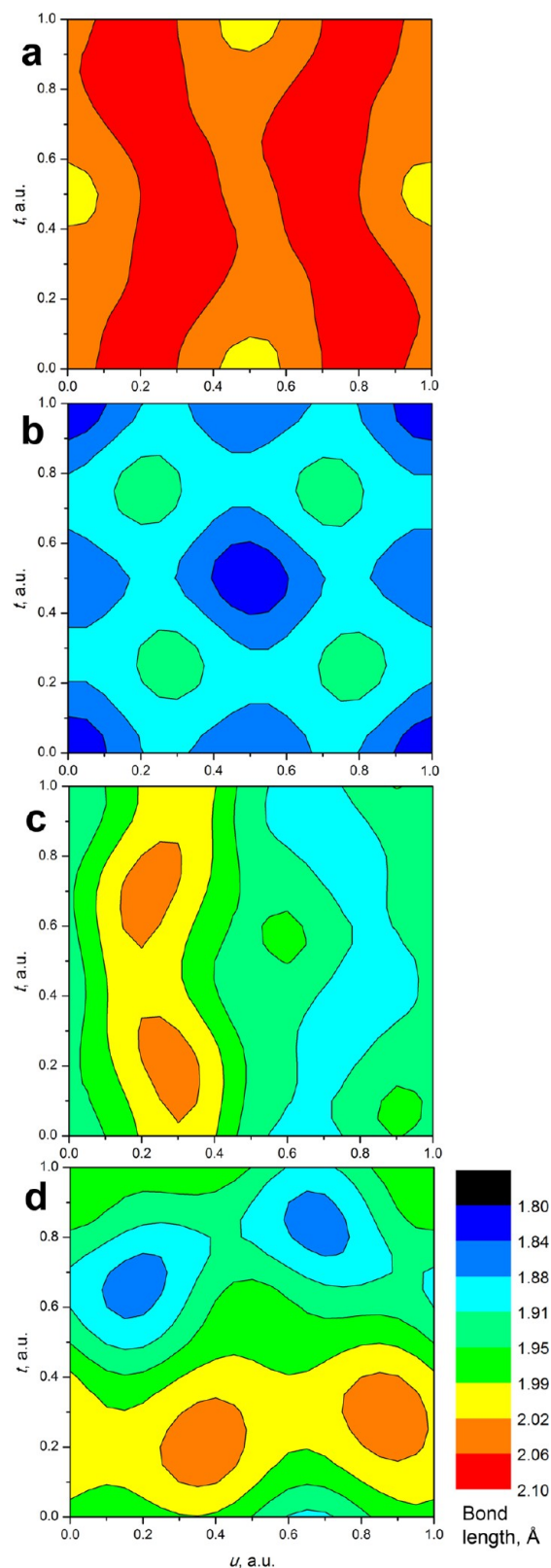


**Figure 9.** Ti–O distances in the  $\text{Li}_{0.15}\text{Nd}_{0.617}\text{TiO}_3$  structure plotted in the  $t$ - $u$  coordinates for the O1 (a), O2 (b), O3 (c), and O4 (d) atoms (atomic positions as given in Figure 5).

## DISCUSSION

Combined results of the TEM, SXPD, and NPD investigation of the  $\text{Li}_{3x}\text{Nd}_{2/3-x}\text{TiO}_3$  perovskites refute the scenario of the



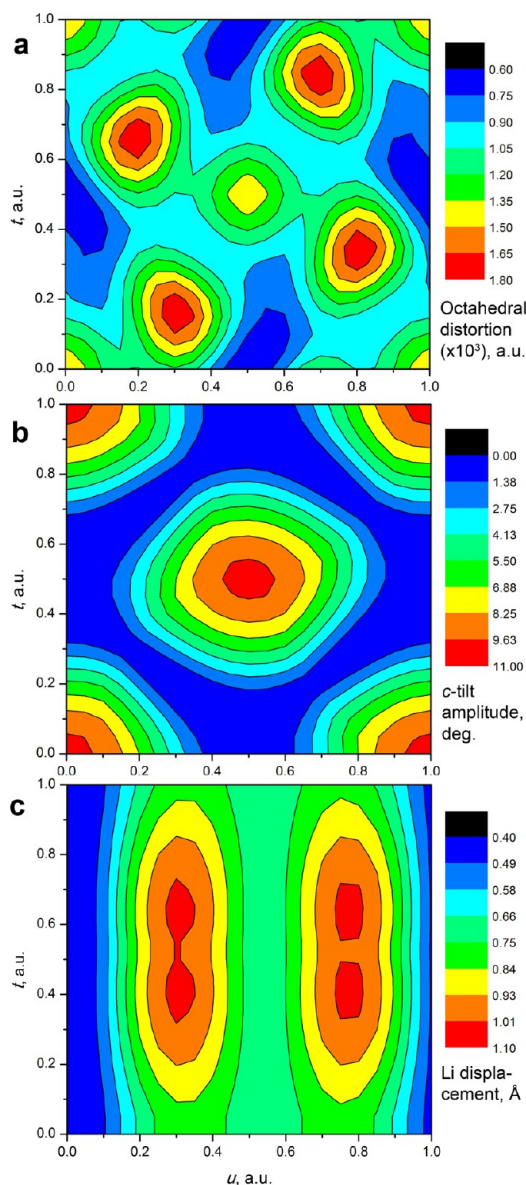


**Figure 10.** Octahedral distortion parameter (a),  $c^+$  tilt amplitude (b), and magnitude of the Li displacement from the ideal 0,0,1/2 position (c) plotted in the  $t$ - $u$  coordinates.

Nd/Li occupancy modulation within the (001) planes and the ensuing nanoscale phase separation into  $\text{Li}_{1/2}\text{Nd}_{1/2}\text{TiO}_3$  and  $\text{Nd}_{2/3}\text{TiO}_3$  domains. Contrarily, our observations favor a structural model based on the purely displacive modulations for several reasons:

- (1) The channeling-induced contrast in [001] BF and ADF-STEM images and its absence in HAADF-STEM images where compositionally induced contrast is expected.
- (2) Satellite reflections related to the phase separation are not observed by SXPD and NPD.
- (3) The satisfactory fit of the intensity of the satellites with displacive modulation functions.
- (4) The agreement between the experimental and calculated [001] ED pattern for the refined  $\text{Li}_{0.15}\text{Nd}_{0.617}\text{TiO}_3$  structure, and the disagreement between experimental and calculated ED patterns based on the model of ref 14.

We can describe the  $\text{Li}_{0.15}\text{Nd}_{0.617}\text{TiO}_3$  structure as a perovskite with frustrated octahedral tilts. Unlike in the

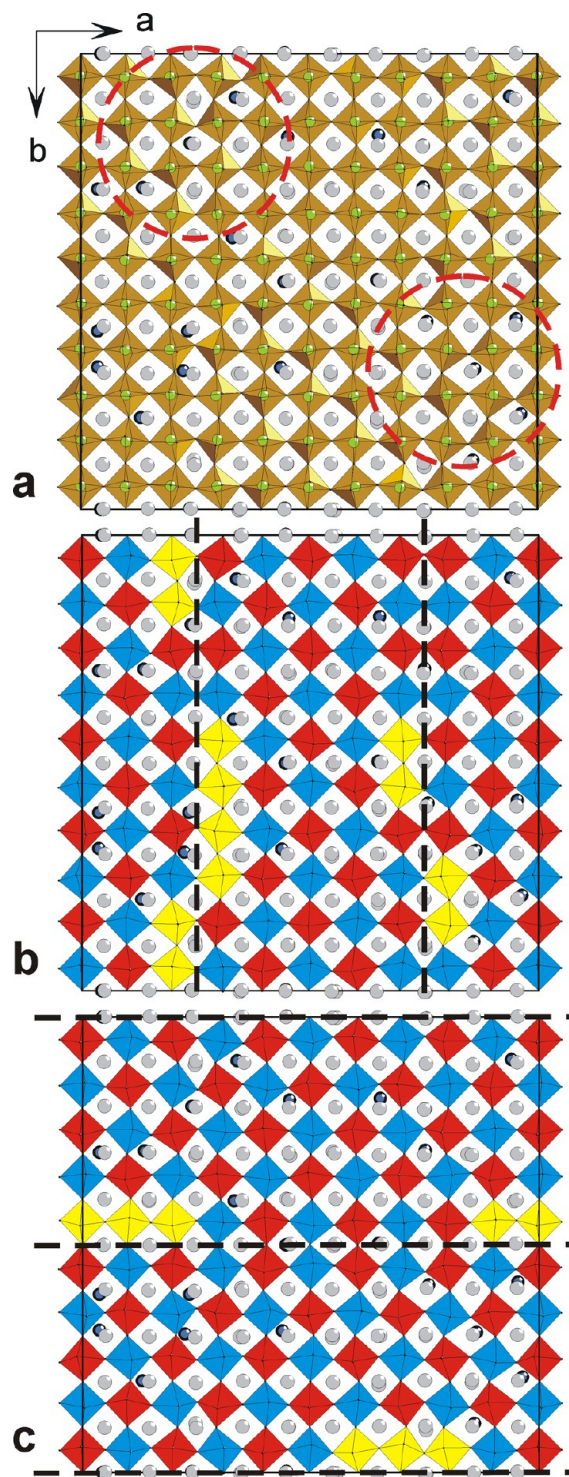


**Figure 11.** Ab initio relaxed  $\text{Li}_{0.125}\text{Nd}_{0.625}\text{TiO}_3$  structure demonstrating the regions with the pronounced tilt of the  $\text{TiO}_6$  octahedra around the  $c$ -axis (a, marked with red circles) and antiphase domains of the  $a^-$  and  $b^-$  tilt components (b and c, separated by black dashed lines). The color scheme is the same as in Figure 7 and 8.

overwhelming majority of distorted perovskites, the octahedral tilts do not keep the same in-phase or out-of-phase relation and equal tilt amplitude throughout the crystal. Instead, the tilt components along the three perovskite cubic directions demonstrate variable tilt amplitudes and even switching between the in-phase and out-of-phase modes. The competi-



tion between the tilt components can be seen from the comparison of Figure 7 and Figure 8: areas with a pronounced  $c^+$  component overlap with areas with dumped  $a^-$  and  $b^-$  components. A primary reason for the tilting distortion is the mismatch between the A–O and B–O interatomic distances, as reflected by the tolerance factor

$$t = \frac{r_A + r_O}{\sqrt{2}(r_B + r_O)} \quad (3)$$

where  $r_A$ ,  $r_B$ ,  $r_O$  are the ionic radii. For the  $\text{Nd}^{3+}$ –O and  $\text{Ti}^{4+}$ –O bonds the mismatch is quantified by the tolerance factor  $t = 0.942$  that already requires a tilting distortion. The tendency toward the tilting distortion is enhanced by the smaller  $\text{Li}^+$  cations that partially replace  $\text{Nd}^{3+}$ . However, instead of regular tilting patterns (for example, those predicted by the group theory analysis of the A-site ordered layered perovskites),<sup>29</sup> a much more complex structure with frustrated octahedral tilts is formed. Therefore, an additional instability must be present in the  $\text{Li}_{3x}\text{Nd}_{2/3-x}\text{TiO}_3$  structure and conspire with the cooperative octahedral tilting to form the frustrated incommensurately modulated structure.

The incommensurate superstructure observed in the  $\text{Li}_{3x}\text{Nd}_{2/3-x}\text{TiO}_3$  perovskites is not unique. Similar modulations have been observed in other perovskites:  $\text{Th}_{1/4}\text{NbO}_3$ ,<sup>38,39</sup>  $\text{Tm}_{1/3}\text{TaO}_3$ ,<sup>40</sup>  $\text{Li}_{3x}\text{La}_{1/3-x}\text{NbO}_3$ ,<sup>41</sup>  $\text{KLaMnWO}_6$  ( $t = 0.986$ ),<sup>42</sup>  $\text{NaLaMgWO}_6$  ( $t = 0.952$ ),<sup>43,44</sup>  $\text{NaNdMgWO}_6$  ( $t = 0.940$ ),<sup>45</sup>  $\text{NaCeMnWO}_6$  ( $t = 0.926$ ),  $\text{NaPrMnWO}_6$  ( $t = 0.924$ ).<sup>46</sup> Three structural features are common to all these compounds:

- A tolerance factor  $t < 1$  indicating an instability toward an octahedral tilting distortion.
- A well established A-site layered ordering of two species, A and A', with a significant charge difference (A, lanthanide cation  $\text{Ln}^{3+}$  or  $\text{Th}^{4+}$ ; A', alkali cation  $\text{M}^+$  or cation vacancy), resulting in a doubling of the perovskite unit cell along the  $c$ -axis.
- The presence of a  $d^0$  transition metal B-cation ( $\text{Ti}^{4+}$ ,  $\text{Nb}^{5+}$ ,  $\text{Ta}^{5+}$ ,  $\text{W}^{6+}$ ) prone to a second-order Jahn–Teller (SOJT) distortion of the  $\text{BO}_6$  octahedra, resulting in the shortening of some of the B–O bonds.

The presence of  $d^0$  cations is vitally important for the stability of the layered A-site ordering. The displacements of these cations toward the oxygen atoms in the (A'O) layer maintain a reasonable bond valence sum for these oxygen atoms. At the same time, the structure gains extra energy from covalent  $\text{nd}^0(\text{B})$ – $2\text{p}(\text{O})$  mixing and antipolar order of the electric dipoles associated with such off-center displacements of the B cations. The energy gain from the dipole–dipole interaction is maximal when the dipoles are directed along the  $c$ -axis and antiparallel to each other, that is, when the octahedral tilting distortion is absent. The tilting, which is required to accommodate small cations in the (AO) layer, destroys the optimal conditions of the  $\text{nd}^0(\text{B})$ – $2\text{p}(\text{O})$  orbital overlap and misaligns the dipoles, thus acting as a competing trend and giving rise to a frustration. A competition between the octahedral tilting and the SOJT distortion is the most likely origin of the incommensurability in such perovskites. The trend of the octahedral tilting preventing (anti)polar instabilities is common in perovskites and may indeed trigger the formation of modulated structures.<sup>2,47,48</sup>

The analysis of the Ti–O distances in  $\text{Li}_{0.15}\text{Nd}_{0.617}\text{TiO}_3$  fully supports this scenario. In this structure, the antipolar displacement of the Ti atoms along the  $c$ -axis does not remain the unique SOJT distortion mode. The established anti-

correlation between the variation of the Ti–O distances in the  $ab$  plane and the  $c^+$  component of the octahedral tilt suggests strong coupling between octahedral tilting and SOJT-driven displacements. The displacement components in the  $ab$  plane compete with the  $c^+$  octahedral tilting component and result in frustrated octahedral tilts, which in turn lead to the displacive incommensurate modulation.

The Li atoms seem to play only an auxiliary role in this modulation. Indeed, similar modulated structures are also formed with larger alkali cations ( $r(\text{Li}^+) = 0.92 \text{ \AA}$ ,  $r(\text{Na}^+) = 1.18 \text{ \AA}$ ,  $r(\text{K}^+) = 1.51 \text{ \AA}$  for CN = 8). The modulation exists even if the alkali cations are absent, as in  $\text{Th}_{1/4}\text{NbO}_3$ ,  $\text{Tm}_{1/3}\text{TaO}_3$ . In the  $\text{Li}_{3x}\text{Nd}_{2/3-x}\text{TiO}_3$  series, the 3-fold increase in the Li content from  $x = 0.05$  to  $x = 0.14$  results only in a slight change of the irrational components of the modulation vectors from 0.436 (as averaged between  $\alpha_1$  and  $\beta_2$ ) to 0.465 (see Supporting Information, Table S2). This clearly demonstrates the weak link between the Li content and the modulation parameters. The primary role of the alkali cations is to stabilize the robust layered ordering of the A and A' cations following the charge difference between +1 and +3, but the same result can be achieved by cation vacancies. The effect of the alkali cations is restricted to the following:

- Tuning of the tolerance factor and energy associated with the octahedral tilting distortion. This effect is corroborated by the clear dependence of the modulation periodicity on the tolerance factor reported for the  $\text{A}'\text{ABWO}_6$  (A = La, Ce, Nd, A' = Na, K, B = Mg, Mn) perovskites.<sup>46</sup>
- A change in the size variance  $\sigma^2(r_A) = \langle r_A^2 \rangle - \langle r_A \rangle^2$  at the A sublattice and the free energy associated with the SOJT distortion. Indeed, a strong influence of the A-site size variance on the ferroelectric Curie temperature was observed in perovskite titanates.<sup>49,50</sup> An increase in the size variance at the A position is likely beneficial for the formation of (3 + 2)-dimensionally modulated (chessboard) structure, whereas similar radii of the A and A' cations would favor the (3 + 1)-dimensional stripe structure.<sup>45</sup> The competition between the chessboard and the stripe patterns can be at the origin of the different satellite broadening associated with the  $\mathbf{q}_1$  and  $\mathbf{q}_2$  vectors in  $\text{Li}_{0.15}\text{Nd}_{0.617}\text{TiO}_3$ , where random perturbations in the modulation wave pertain to the  $\mathbf{q}_1$  vector. Such perturbations can be considered as an intermediate state between the (3 + 2)D (chessboard) and (3 + 1)D (stripe) modulated structure.

Thus, one can suspect that the tolerance factor and the A-site size variance may underlie the compositional dependence of the modulation vector in the  $\text{Li}_{3x}\text{Nd}_{2/3-x}\text{TiO}_3$  perovskites, as well as the appearance of the incommensurate modulation upon Li doping in  $\text{La}_{1/3}\text{NbO}_3$ .<sup>41</sup> However, deciphering the relative impacts of these factors will require quantitative crystallographic data on other representatives of this perovskite family.

The link between the modulated octahedral tilts and cation ordering in the (Nd<sub>2</sub>,Li)O<sub>2</sub> layer was additionally verified by ab initio structure relaxation. In the starting model with the  $\text{Li}_{0.125}\text{Nd}_{0.625}\text{TiO}_3$  composition,  $10a_p \times 10a_p \times 2a_p$  unit cell and  $P11m$  space symmetry all atoms are free to move in the  $ab$  plane and the displacements along the  $c$ -axis are restricted by the  $m_z$  mirror plane. The cation positions in the (Nd<sub>2</sub>,Li)O<sub>2</sub> layer were randomly populated by Nd, Li, and vacancies to maintain the chemical composition. Despite the absence of any cation ordering within the (001) planes, the relaxed structure reproduces fairly well the main features of the modulated octahedral tilts in the refined  $\text{Li}_{0.15}\text{Nd}_{0.617}\text{TiO}_3$  structure (Figure 11). Areas with a pronounced and suppressed  $c^+$  tilt

component are clearly present in the relaxed structure (Figure 11a). Areas with  $a^-$  and  $b^-$  tilts are split into domains separated by APBs parallel to (100) and (010) lattice planes, respectively (Figure 11b,c). The domains appear to be quite sharp (Supporting Information, Figure S9) and reminiscent of those observed on the HRTEM images. However, the harmonic or step-like behavior of the atomic displacements can not be unambiguously resolved from the relaxed structure. Similar to the refined structure, the Nd2 atoms demonstrate only small shifts from their ideal positions at the center of the perovskite cube, whereas the Li atoms are significantly shifted in the  $ab$  plane. In both the refined and the relaxed structures, the Li atoms never sit exactly at the square oxygen window formed by four  $\text{TiO}_6$  octahedra. Moreover, the preferential displacement direction is not only toward the square window (i.e.,  $\langle 100 \rangle_p$  direction), but also toward the  $\langle 110 \rangle_p$  directions.

The relaxation was also performed for a model with an ordered arrangement of Li, Nd, and vacancies. The composition and crystallographic parameters were kept the same as for the disordered structure, but cations and vacancies were distributed in the  $(\text{Nd}_2\text{Li})\text{O}_2$  layer in an ordered manner following the most homogeneous two-dimensional ordering patterns.<sup>51</sup> An essentially similar scenario of octahedral tilts and cation displacements was obtained, and only a marginal energy difference with respect to the structure with disordered cation arrangement was observed. Therefore, the displacive modulated tilting pattern of the  $\text{TiO}_6$  octahedra is energetically favorable and remains relatively insensitive to the cation and vacancy ordering at the A site. This strongly supports the TEM and Rietveld refinement results, where no cation ordering in the  $(\text{Nd}_2\text{Li})\text{O}_2$  layer has been detected.

The above consideration doubts the existence of a compositional phase separation in other layered A-site ordered perovskites with incommensurate superstructures, which are strikingly similar to that in  $\text{Li}_{3x}\text{Nd}_{2/3-x}\text{TiO}_3$ . The chemical composition of these perovskites is not in line with the proposed compositional phase separation. In  $\text{Li}_{3x}\text{Nd}_{2/3-x}\text{TiO}_3$  the cation positions in the  $(\text{A}'\text{O})$  layer are taken by three species with different formal charges: lanthanide cation (charge +3), lithium cation (charge +1), and cation vacancy (charge 0). By combining these three species in different ratios, it is easy to construct distinct chemical compositions for the phase separated domains, while maintaining the electroneutrality of each phase and the bulk sample composition. However, this approach fails for such perovskites as  $\text{A}'\text{ABWO}_6$  ( $\text{A} = \text{La}, \text{Ce}, \text{Nd}, \text{A}' = \text{Na}, \text{K}, \text{B} = \text{Mg}, \text{Mn}$ ).<sup>42–46</sup> Here, the attempts to explain the modulated structure by an underlying compositional phase separation unavoidably lead to an unjustified alteration of the overall cation content. For  $\text{NaLaMgWO}_6$ , the compositions of the phase-separated domains were proposed to be  $\text{La}(\text{Na}_{1-3x}\text{La}_x)\text{MgWO}_6$  and  $\text{NaLaMgWO}_6$ , which results in a significant deviation of the bulk composition of such phase-separated system from the nominal  $\text{NaLaMgWO}_6$ . The  $\text{Na}_{5/8}\text{La}_{9/8}\square_{1/4}\text{MgWO}_6$  and  $\text{Na}_{1/2}\text{La}_{7/6}\square_{1/3}\text{MgWO}_6$  ( $\square$ , cation vacancy) formulas were suggested corresponding to 37–50% Na loss.<sup>43,44</sup> Attempts to prepare the  $\text{La}(\text{Na}_{1-3x}\text{La}_x)\text{MgWO}_6$  solid solution resulted in samples whose XRD patterns show extremely subtle changes, and the lattice parameters do not vary systematically with the composition. The periodicity of the incommensurate modulation (revealed from transmission electron microscopy) does not noticeably depend on the  $x$  value in  $\text{La}(\text{Na}_{1-3x}\text{La}_x)\text{MgWO}_6$  thus suggesting that the modulation is not of compositional origin.<sup>44</sup> Indeed, refinement

of the Na/La occupancy variation using the supercell approach did not give a significant change of the Rietveld fit of the neutron powder diffraction data.<sup>43</sup> The argument that the bulk composition of the phase-separated material deviates from the nominal one owing to exsolution of the  $\text{Na}_2\text{WO}_4$  impurity seems to be implausible. For example, modulated  $\text{NaCeMnWO}_6$  and  $\text{NaPrMnWO}_6$  can be prepared either in pure form or with <1 mol % of  $\text{Na}_2\text{WO}_4$ ,<sup>46,52</sup> that is insufficient to explain the compositional changes required by the hypothesis of a phase separation. However, it should be noted that although the above consideration points toward the absence of a compositional modulation, nanometer-scale mapping of the La concentration with electron energy loss spectroscopy (EELS) in  $\text{NaLaMgWO}_6$  and  $\text{KLaMnWO}_6$  demonstrates a variation of the La content with a periodicity matching that of the incommensurate modulation, thus causing an unresolved controversy.<sup>42,44</sup> Yet, the interpretation of EELS data in terms of chemical composition (qualitative or quantitative) can be misleading in the presence of severe diffraction effects, particularly if a small collection aperture is used.<sup>53,54</sup>

Observation of the same type of modulation in the  $\text{Tm}_{1/3}\text{TaO}_3$  perovskite also points against a compositional phase separation.<sup>40</sup> A modulation of the Tm occupancy would result in  $\text{Tm}_{1/3-\delta}\text{TaO}_3$  and  $\text{Tm}_{1/3+\delta}\text{TaO}_3$  domains. This would violate the local electroneutrality, unless it is compensated by oxygen or tantalum deficiency, which is very unlikely. These facts, combined with the present structural investigation on  $\text{Li}_{3x}\text{Nd}_{2/3-x}\text{TiO}_3$ , call for a critical revision of the compositional phase separation scenario in these perovskites.

Finally, we comment on the dielectric properties of  $\text{Li}_{3x}\text{Nd}_{2/3-x}\text{TiO}_3$  and related perovskites. According to the recent computational work,<sup>10,55,56</sup> the combination of the  $a^-a^-c^+$  octahedral tilt system and layered A-site cation ordering can be used to design new materials, which have been coined hybrid improper ferroelectrics. Electric polarization in these materials could be induced by an uncompensated displacement of the A and A' cations in neighboring layers. However, our experimental results pinpoint the high complexity of the relevant crystal structures that feature a welter of octahedral tilting modes and distortion modes related to the B-cation displacements. A full description of these modes is yet to be done in a DFT-based microscopic analysis. Presently, we note that the  $\text{Li}_{3x}\text{Nd}_{2/3-x}\text{TiO}_3$  structure is nonpolar, in spite of large displacements of the Li atoms that are randomly distributed on both sides of the  $m_x$  mirror plane. Nevertheless, the structure may become polar on a local scale, provided that one of the two symmetrically equivalent positions is preferentially occupied, as shown in Figure 7, where only one Li position is drawn. This local order of Li atoms may be related to polar clusters in  $\text{Li}_{0.3}\text{Nd}_{0.567}\text{TiO}_3$ , as reported by Withers et al.<sup>16</sup> An important outcome of our work is the lack of macroscopic polarity in  $\text{Li}_{3x}\text{Nd}_{2/3-x}\text{TiO}_3$  and, presumably, in related perovskite titanates. One can expect that in these compounds polarity may emerge only locally.

## CONCLUSIONS

Using a combination of transmission electron microscopy, synchrotron X-ray powder diffraction, neutron powder diffraction, and ab initio structure relaxations we have demonstrated that the compositional nanoscale phase separation into  $\text{Nd}_{2/3}\text{TiO}_3$  and  $\text{Li}_{1/2}\text{Nd}_{1/2}\text{TiO}_3$  domains is absent in the  $\text{Li}_{3x}\text{Nd}_{2/3-x}\text{TiO}_3$  perovskites. Being restricted by the limitations of the experimental and computational methods,



we, nevertheless, have obtained a first approximation of the complex displacively modulated structure of these materials. In agreement with the early hypothesis from García-Martín et al.,<sup>13</sup> the modulation involves a fragmentation of the  $a^-b^-c^0$  tilt system of the  $\text{TiO}_6$  octahedra into domains that are in antiphase relation to each other. This ordering is superimposed on the pattern of the domains with either a well pronounced or suppressed  $c^+$  octahedral tilt component. The octahedral tilting competes with a second-order Jahn–Teller distortion of the  $\text{TiO}_6$  octahedra, thus giving rise to a modulated structure. The A cations affect it through changing the tolerance factor and, probably, the size variance. Ab initio structure optimization demonstrates that the modulated structure is stable without the underlying nanoscale phase separation. These findings doubt the compositional phase separation scenario proposed for similar incommensurately modulated layered A-site ordered perovskites. Further progress in understanding these extremely complex structures requires the preparation of these materials in the form of single crystals. Single crystal diffraction experiments should allow accessing the high order satellites and resolving the detailed structure of the domain boundaries.

## ■ ASSOCIATED CONTENT

### ■ Supporting Information

EDX results, unit cell parameters, and irrational components of the modulation vectors, illustration of multiple diffraction paths, simulated [001] BF-STEM and HAADF-STEM images for the model of Guiton and Davies, experimental BF-, ABF-, and HAADF-STEM images for  $\text{Li}_{0.15}\text{Nd}_{0.617}\text{TiO}_3$  and  $\text{Li}_{0.36}\text{Nd}_{0.547}\text{TiO}_3$ , calculated and experimental [001] ED patterns, HRTEM, BF-, ADF-, and HAADF-STEM images for  $\text{Li}_{0.15}\text{Nd}_{0.617}\text{TiO}_3$ , reliability factors for tested superspace groups, symmetry operators of the superspace group, atomic coordinates, amplitudes of Fourier components for the displacive modulation functions, isotropic atomic displacement parameters, and main interatomic distances for  $\text{Li}_{0.15}\text{Nd}_{0.617}\text{TiO}_3$ , atomic coordinates and bond valence sums for the ab initio relaxed  $\text{Li}_{0.125}\text{Nd}_{0.625}\text{TiO}_3$  structure, mapping of atomic displacements in the relaxed structure, CIF files for the refined and relaxed structures. This material is available free of charge via the Internet at <http://pubs.acs.org>.

## ■ AUTHOR INFORMATION

### Corresponding Author

\*E-mail: [artem.abakumov@ua.ac.be](mailto:artem.abakumov@ua.ac.be).

### Notes

The authors declare no competing financial interest.

## ■ ACKNOWLEDGMENTS

We are grateful to the ESRF and ILL for granting the beamtime. Experimental support of Andy Fitch at the ID31 beamline of ESRF is kindly acknowledged. Part of this work was supported by funding from the European Research Council under the seventh Framework Program (FP7), ERC Grant No. 246791–COUNTATOMS and from the European Social Fund under the Mobilitas Grant MTT77.

## ■ REFERENCES

- (1) Mitchell, R. H. *Perovskites: Modern and Ancient*; Almaz Press Inc: Thunder Bay, Canada, 2002.
- (2) Kim, J.-W.; Thompson, P.; Brown, S.; Normile, P. S.; Schlueter, J. A.; Shkabko, A.; Weidenkaff, A.; Ryan, P. J. *Phys. Rev. Lett.* **2013**, *110*, 027201.
- (3) Rusakov, D. A.; Abakumov, A. M.; Yamaura, K.; Belik, A. A.; Van Tendeloo, G.; Takayama-Muromachi, E. *Chem. Mater.* **2011**, *23*, 285–292.
- (4) Blinc, R.; Laguta, V.; Zalar, B. *Phys. Rev. Lett.* **2003**, *91*, 247601.
- (5) King, G.; Woodward, P. M. *J. Mater. Chem.* **2010**, *20*, 5785–5796.
- (6) Knapp, M. C.; Woodward, P. M. *J. Solid State Chem.* **2006**, *179*, 1065–1074.
- (7) Inaguma, Y.; Liquan, C.; Itoh, M.; Nakamura, T.; Uchida, T.; Ikuto, H.; Wakihara, M. *Solid State Commun.* **1993**, *86*, 689–693.
- (8) Takahashi, H.; Baba, Y.; Ezaki, K.; Okamoto, Y.; Shibata, K.; Kuroki, K.; Nakano, S. *Jpn. J. Appl. Phys.* **1991**, *30*, 2339–2342.
- (9) King, G.; Thimmaiah, S.; Dwivedi, A.; Woodward, P. M. *Chem. Mater.* **2007**, *19*, 6451–6458.
- (10) Fukushima, T.; Stroppa, A.; Picozzi, S.; Perez-Mato, J. M. *Phys. Chem. Chem. Phys.* **2011**, *13*, 12186–12190.
- (11) Guiton, B. S.; Davies, P. K. *Nat. Mater.* **2007**, *6*, 586–591.
- (12) Robertson, A. D.; García-Martín, S.; Coats, A.; West, A. R. *J. Mater. Chem.* **1995**, *5*, 1405–1412.
- (13) García-Martín, S.; García-Alvarado, F.; Robertson, A. D.; West, A. R.; Alario-Franco, M. A. *J. Solid State Chem.* **1997**, *128*, 97–101.
- (14) Guiton, B. S.; Wu, H.; Davies, P. K. *Chem. Mater.* **2008**, *20*, 2860–2862.
- (15) Lu, J. B.; Yang, H. X.; Li, Z. A.; Ma, C.; Shi, H. L.; Zeng, L. J.; Li, J. Q. *J. Solid State Chem.* **2008**, *181*, 3194–3199.
- (16) Withers, R. L.; Bourgeois, L.; Snashall, A.; Liu, Y.; Noren, L.; Dwyer, C.; Etheridge, J. *Chem. Mater.* **2013**, *25*, 190–201.
- (17) Petricek, V.; Dusek, M.; Palatinus, L. *Jana2006, The crystallographic computing system*; Institute of Physics: Praha, Czech Republic, 2006.
- (18) Kresse, G.; Furthmüller, J. *Comput. Mater. Sci.* **1996**, *6*, 15–50.
- (19) Kresse, G.; Furthmüller, J. *Phys. Rev. B* **1996**, *54*, 11169–11186.
- (20) Blöchl, P. E. *Phys. Rev. B* **1994**, *50*, 17953–17979.
- (21) Kresse, G.; Joubert, D. *Phys. Rev. B* **1999**, *59*, 1758–1775.
- (22) Perdew, J. P.; Burke, K.; Ernzerhof, M. *Phys. Rev. Lett.* **1996**, *77*, 3865–3868.
- (23) Gonzalez, S.; Perez-Mato, J. M.; Elcoro, L.; Garcia, A.; Withers, R. L.; Bourgeois, L. *J. Phys.: Condens. Matter.* **2012**, *24*, 495301.
- (24) Erni, R.; Abakumov, A. M.; Rossell, M. D.; Batuk, D.; Tsirlin, A. A.; Nénert, G.; Van Tendeloo, G. *Nat. Mater.* **2013**, submitted for publication.
- (25) Matsumura, S.; Toyohara, M.; Tomokiyo, Y. *Philos. Mag. A* **1990**, *62*, 653–670.
- (26) van Smaalen, S.; Campbell, B. J.; Stokes, H. T. *Acta Crystallogr.* **2013**, *A69*, 75–90.
- (27) Alonso, J. A.; Sanz, J.; Santamaría, J.; León, C.; Várez, A.; Fernández-Díaz, M. T. *Angew. Chem., Int. Ed.* **2000**, *39*, 619–621.
- (28) Sommariva, M.; Catti, M. *Chem. Mater.* **2006**, *18*, 2411–2417.
- (29) Howard, C. J.; Zhang, Z. *J. Phys.: Condens. Matter.* **2003**, *15*, 4543–4553.
- (30) Van Tendeloo, G.; Amelinckx, S. *Acta Crystallogr., Sect. A* **1974**, *30*, 431–440.
- (31) Boulesteix, C.; Van Landuyt, J.; Amelinckx, S. *Phys. Status Solidi A* **1976**, *33*, 595–606.
- (32) Bougerol, C.; Gorius, M.; Grey, I. *J. Solid State Chem.* **2002**, *169*, 131–138.
- (33) Abakumov, A. M.; Hadermann, J.; Bals, S.; Nikolaev, I. V.; Antipov, E. V.; Van Tendeloo, G. *Angew. Chem.* **2006**, *45*, 6697–6700.
- (34) Abakumov, A. M.; Hadermann, J.; Van Tendeloo, G.; Antipov, E. V. *J. Am. Ceram. Soc.* **2008**, *91*, 1807–1813.
- (35) Abakumov, A. M.; Batuk, D.; Hadermann, J.; Rozova, M. G.; Sheptyakov, D. V.; Tsirlin, A. A.; Niermann, D.; Waschkowski, F.; Hemberger, J.; Van Tendeloo, G.; Antipov, E. V. *Chem. Mater.* **2011**, *23*, 255–265.
- (36) Van Smaalen, S. *Incommensurate Crystallography*; Oxford University Press, New York, 2007; pp 38–43.
- (37) Brown, I. D.; Shannon, R. D. *Acta Crystallogr., Sect. A* **1973**, *29*, 266–282.

- (38) Alario-Franco, M. A.; Grey, I. E.; Joubert, J. C.; Vincent, H.; Labeau, M. *Acta Crystallogr., Sect. A* **1982**, *38*, 177–186.
- (39) Labeau, M.; Grey, I. E.; Joubert, J. C.; Vincent, H.; Alario-Franco, M. A. *Acta Crystallogr., Sect. A* **1982**, *38*, 753–761.
- (40) Zhou, Q.; Saines, P. J.; Sharma, N.; Ting, J.; Kennedy, B. J.; Zhang, Z.; Withers, R. L.; Wallwork, K. S. *Chem. Mater.* **2008**, *20*, 6666–6676.
- (41) García-Martín, S.; Alario-Franco, M. A. *J. Solid State Chem.* **1999**, *148*, 93–99.
- (42) García-Martín, S.; King, G.; Urones-Garrote, E.; Nénert, G.; P.M. Woodward, P. M. *Chem. Mater.* **2011**, *23*, 163–170.
- (43) King, G.; García-Martín, S.; Woodward, P. M. *Acta Crystallogr., Sect. B* **2009**, *65*, 676–683.
- (44) García-Martín, S.; Urones-Garrote, E.; Knapp, M. C.; King, G.; Woodward, P. M. *J. Am. Chem. Soc.* **2008**, *130*, 15028–15037.
- (45) Licurse, M. W.; Davies, P. K. *Appl. Phys. Lett.* **2010**, *97*, 123101.
- (46) García-Martín, S.; King, G.; Nénert, G.; Ritter, C.; Woodward, P. M. *Inorg. Chem.* **2012**, *51*, 4007–4014.
- (47) King-Smith, R. D.; Vanderbilt, D. *Phys. Rev. B* **1994**, *49*, 5828–5844.
- (48) Zhong, W.; Vanderbilt, D. *Phys. Rev. Lett.* **1995**, *74*, 2587–2590.
- (49) Attfield, J. P. *Int. J. Inorg. Mater.* **2001**, *3*, 1147–1152.
- (50) Sinclair, D. C.; Attfield, J. P. *Chem. Commun.* **1999**, 1497–1498.
- (51) Gonzalez, S.; Perez-Mato, J. M.; Elcoro, L.; Garcia, A. *Phys. Rev. B* **2011**, *84*, 184106.
- (52) King, G.; Wayman, L. M.; Woodward, P. M. *J. Solid State Chem.* **2009**, *182*, 1319–1325.
- (53) Muller, D. A.; Kourkoutis, L. F.; Murfitt, M.; Song, J. H.; Hwang, H. Y.; Silcox, J.; Dellby, N.; Krivanek, O. L. *Microsc. Microanal.* **2008**, *14* (Suppl. 2), 132–133.
- (54) Bosman, M.; Keast, V. J.; Garcia-Munoz, J. L.; D'Alfonso, A. J.; Findlay, S. D.; Allen, L. J. *Phys. Rev. Lett.* **2007**, *99*, 086102.
- (55) Rondinelli, J. M.; Fennie, C. J. *Adv. Mater.* **2012**, *24*, 1961–1968.
- (56) Benedek, N. A.; Mulder, A. T.; Fennie, C. J. *J. Solid State Chem.* **2012**, *195*, 11–20.